Supplemental Material for "A description of turbulent wall-flow vorticity consistent with mean dynamics"

By J. C. KLEWICKI[1,2]

[1]Department of Mechanical Engineering, University of Melbourne, Melbourne, VIC 3010, Australia

[2]Department of Mechanical Engineering, University of New Hampshire, Durham, NH 03824, USA

(Received ?? and in revised form ??)

1. Introduction

This supplemental material augments and reinforces the analyses and results presented in the primary manuscript.

2. Results

Herein, results are presented in the same order as in the accompanying manuscript. Figure, table and equation numbers followed by an "m" refer to those appearing in the manuscript.

2.1. *Mean Vorticity Field Development*

This section first examines how the integral property of displacement thickness develops with δ^+. The subsequent analyses then examine the scaling behaviours of the Ω_z profiles.

2.1.1. *Displacement Thickness*

Figure 1 presents δ^*/δ versus δ^+ using the data sets listed in table 2m. For reference, the value for the laminar solution for fully developed pipe flow is plotted at $\delta^+ = 30$. The onset of the four layer regime for each flow is indicated by a vertical dotted line. These δ^+ values were determined by Elsnab et al. (2011); Klewicki et al. (2011) and Klewicki et al. (2012). Although each is different in detail, the profiles in figure 1 share a number of qualitative features. Each drops precipitously through the transitional regime. Each profile also exhibits a distinctive change in slope near the onset of the four layer regime. The channel and pipe profiles transition from a steeply downward to a more gradually downward slope. For the boundary layer, the change in slope is more dramatic; from a steeply downward slope to at least a plateau, and even possibly to a slightly upward slope for a small range of δ^+. The scatter in the boundary layer data is, however, noticeably higher than either the pipe or channel data.

Higher scatter is also seen for the boundary layer data of figure 5 below. This is most likely a consequence of the more delicate manner by which the boundary layer vorticity field develops. That is, the boundary layer has neither a mean flux of vorticity from the wall, nor an inherent annihilation of mean vorticity in the outer region; both of which are present in the channel and the pipe. In addition, boundary layers are bounded

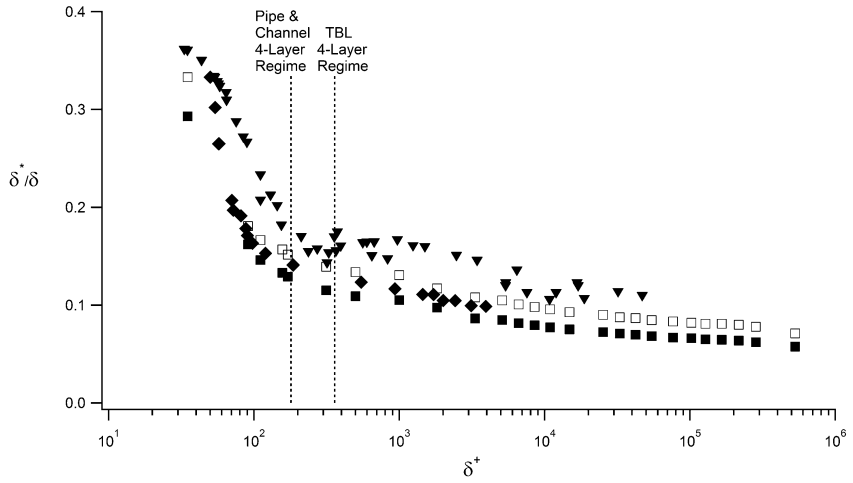

FIGURE 1. Outer normalized displacement thickness as a function of δ^+, boundary layer, ▼; channel, ♦; pipe, ■; profile found by using the pipe flow data in (3.1m), □.

by an (essentially) irrotational freestream, and thus their dynamics involve entrainment processes not present in pipes or channels.

Once within the four layer regime, the profiles maintain a plateau-like character, and then exhibit another change in slope. For the channel, this change is subtle, but appears to exhibit a slightly steeper downward trend starting near $\delta^+ = 1500$. For the pipe the region of steeper slope is more distinct; starting near $\delta^+ = 2000$ and completing near $\delta^+ = 3000$. Beyond its elevated plateau between $400 \lesssim \delta^+ \lesssim 2000$ the boundary layer data exhibit a more smoothly decreasing trend – to within the data scatter.

At any given Reynolds number, the δ^*/δ values are consistently largest in the boundary layer, followed by the channel, and then the pipe. Both the total amount of outer region vorticity (circulation/length) and the geometry of the flow influence this trend. Comparison of figure 6m with figures 4 and 5 herein indicates that the boundary layer proportionally contains the largest amount outer region vorticity at any given δ^+. This naturally causes the centroid of mean vorticity to reside at a larger wall-normal location. The channel and boundary layer δ^*/δ profiles have been verified to nominally merge if they are weighted by a measure of this outer region $|\Omega_z|$, e.g., the inverse of their respective $U_e^+ - U_{W_{max}}^+$ values from table 3m.

The pipe flow $U_e^+ - U_{W_{max}}^+$ entry in table 3m is between that for the channel and boundary layer, and thus this explanation leads to the expectation that the pipe flow δ^*/δ profile should also fall between the other two. The pipe profile, however, is also influenced by its geometry, as indicated by the radial weighting in the integral of (3.2m). Effectively, there is more volume per unit circular arc near the outer wall than near the pipe centerline. Thus, more of the total amount of spanwise vorticity concentrates nearer to the wall through transition, and into the four layer regime. This results in the observed lower values for the pipe profile. A test of this explanation is made by using the pipe flow mean velocity profile data in the δ^*/δ equation appropriate for a rectangular geometry, (3.1m). The net result is shown by the open symbols in figure 1. As expected, this "pipe profile" now resides between the channel boundary layer profiles.

2.1.2. *Mean Vorticity Contributions to δ^**

A combination of theoretical predictions and empirical quantifications respectively allows one to construct approximate formulae for the displacement thickness, δ^*, for each of the canonical flows studied herein. An attractive attribute of this formulation is that it reveals the contributions to δ^* from each of the inner and outer self-similar domains on the L_β hierarchy (figures 1m - 3m), as well as from the flow domains that are interior to and beyond the lower and upper boundaries of the hierarchy.

The approximate equations are based upon the vorticity formulation for δ^*, which for rectangular geometries is given by

$$\delta^* = \frac{\int_0^\delta y\Omega_z dy}{\int_0^\delta \Omega_z dy}. \tag{2.1}$$

Noting that the denominator of (2.1) is the total circulation per unit length, $\Gamma_\infty = -U_\infty$ (or $\Gamma_c = -U_c$), the task is thus to develop expressions for the numerator on the following domains,

(a) from the wall to the onset of the hierarchy ($0 \leqslant y^+ \lesssim 7$),

(b) layer II ($7 \lesssim y^+ \lesssim 1.6\sqrt{\delta^+}$),

(c) between the top of layer II and the end of the hierarchy ($1.6\sqrt{\delta^+} \lesssim y^+ \lesssim \delta^+/2$), and

(d) between the top of the hierarchy and the freestream or centerline ($1/2 \lesssim y/\delta \lesssim 1$).

The centroid of region (a) is readily estimated by noting that Ω_z is approximately constant between $0 \leqslant y^+ \lesssim 7$. The wall value is used in the present equations, and thus slightly over-estimates this contribution. The near-wall curve-fit of figure 7 over the lower portion of layer II is well-approximated by $|\Omega_z^+| = 25.4(y^+)^{-\phi_c}$, where $\phi_c = 1.6$. This is the expression used for the region (b) contribution, although it is recognized that as δ^+ becomes large, the use of this function results in an under-estimation of the net contribution. For region (c) the theoretical prediction, $|\Omega_z^+|\epsilon^{-1} = \phi_c^2(\epsilon y^+)^{-1}$ is employed (see figure 7). This equation also slightly under-estimates the true value at low δ^+, but becomes increasingly accurate with increasing δ^+. Between $y/\delta = 0.5$ and $y/\delta = 1$ (region d), the theory informs us that $|\Omega_z^+|$ scales like a constant times ϵ^2, with the magnitude of the constant reflecting the actual rate of $|\Omega_z|$ decay.

The same value of $\phi_c = 1.6$ was used for each flow. This is based upon the theoretically based expectation that the values of ϕ_c in each flow will become closer to each other as δ^+ increases. In each case, the region (d) constant was chosen to shift the overall result such that it reasonably matched the data shown in figure 2. No special effort was made to optimize the fit. On physical grounds, however, the constant is expected to be close to the respective value of $dU^+/d\eta|_{W_{max}}$ in table 3m. This was borne-out by the results, with the constant, C_1, equaling 3.5, 7.2, and 6.6 for the channel, pipe, and boundary layer, respectively. Upon performing the integrations, the resulting equation for the inner-normalized displacement thickness in the channel and boundary layer is given by

$$\delta^{*+} = \frac{49/2}{U_e^+} + \frac{25.4(1.2\delta^{+0.2} - 2.18)}{U_e^+} + \frac{2.56(\delta^+/2 - 1.6\sqrt{\delta^+})}{U_e^+} + \frac{3/8C_1\delta^+}{U_e^+}. \tag{2.2}$$

The four terms on the right respectively represent the contributions (a)-(d) listed above, with the difference between these two flows reflected in the value of C_1. Owing to the circular geometry, the corresponding equation for the pipe has a significantly larger number of terms (in both the numerator and denominator), and thus is not presented here. The

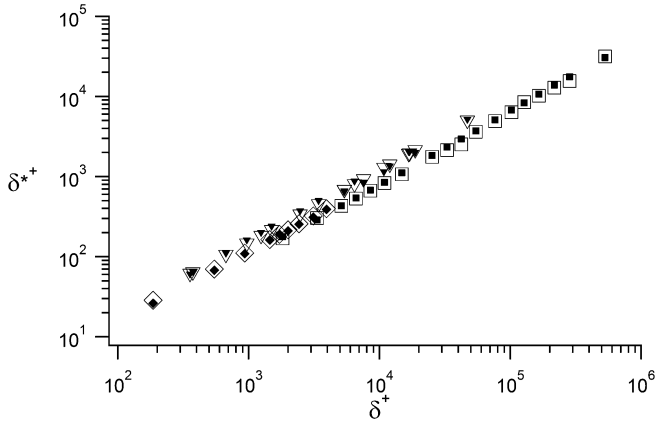

FIGURE 2. Inner-normalized displacement thickness for channels, pipes and boundary layers versus δ^+. Solid symbols are the inner-normalized data from figure 1. Open symbols are from approximate formulation, e.g., (2.2).

open symbols in figure 2 show the results from the approximate formulation as a function of δ^+, while the actual data are given by the smaller solid symbols. As can be seen, in all cases the agreement between the approximate equation and the measured values of δ^{*+} is very good.

Figure 2 rather strongly suggests that a power function fit to the data would yield a compact and reasonably accurate representation of δ^{*+} as a function of δ^+. The advantage of (2.2), however, is that it allows one to examine the (a)-(d) contributions to δ^{*+}. These contributions are respectively shown for the channel and the boundary layer in figures 3a,b.

The data of figure 3a for the channel shows that for increasing δ^+ contribution (d) rapidly levels-off at 1/2 of the total. At the onset of the four layer regime, contribution (c) is about 35%, and approaches 50% as δ^+ increases. These attributes of contributions (c) and (d) with increasing δ^+ are consistent with the approximate symmetry properties of the channel flow Ω_z profile about $\eta = y/\delta = 0.5$ recently noted by Laadhari (2011). Contributions (a) and (b) diminish as δ^+ increases. At $\delta^+ = 3941$, contribution (a) accounts for about 0.25%, while contribution (b) amounts to about 2.5% of the total. At this Reynolds number, contribution (b) is slightly under-estimated. The overall contribution of this term decreases with increasing δ^+, and thus the parity between (c) and (d) emerges slightly more slowly than depicted in figure 3a.

The boundary layer data of figure 3b exhibit similarities, but are distinct from those for the channel. Like in the channel, the fractional contribution from term (d) is nearly constant for all δ^+, but in this case it accounts for about 2/3 of the total. Similarly, contribution (c) rises up with increasing δ^+ to account for nearly all of the remainder. At $\delta^+ \simeq 47000$, contributions from regions (a)-(d) are about 0.015%, 0.3%, 34%, and 66%, respectively. Again, the actual drop-off in contribution (b) is reasoned to be not quite as fast as estimated.

The results of figures 3a,b reveal that the structural differences between channels and boundary layers are not always subtle. They also reinforce the observation that the development of the vorticity distribution in layer IV is a primary difference between the canonical flows. The emergence of Reynolds number invariant contributions from region (c) and the rapidly constant contribution from region (d) indicates that the vorticity distribution inherently adjusts such that the effect of increasing domain size compensates

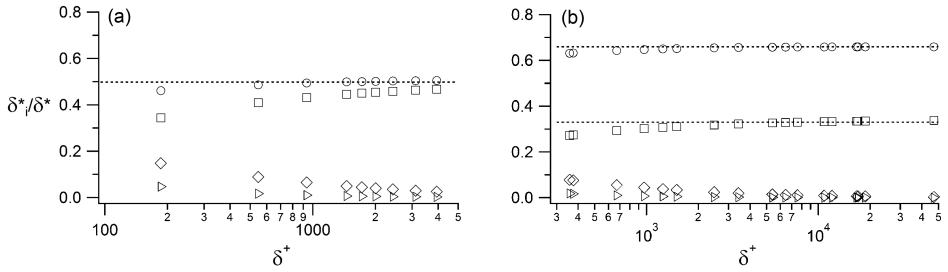

FIGURE 3. Fractional contributions from regions (a)-(d) to δ^{*+} in (a) channels and (b) boundary layers: region (a), ▷; region (b), ◇; region (c), □; region (d), ○.

for the decreasing vorticity magnitude so as to keep the contribution to (2.2) from the outer half of the flow essentially constant. These properties provide insight regarding the success of the displacement thickness weighted outer-normalization proposed by Zagarola & Smits (1998b). Lastly, it is useful to bear in mind that the position where $\Gamma = \Gamma_\infty/2$ resides near the outer edge of layer II, and thus the initial 50% of the circulation (per unit length) becomes concentrated very close to the wall relative to δ^* as δ^+ increases.

2.1.3. *Scaling Behaviours of the* Ω_z *Profile*

Figures 4 and 5 augment the pipe flow data of figure 6m. In each case it is observed that these measures of the vorticity distribution in the outer part of layer IV do not settle into approximately constant values until well after the onset of the four layer regime. This is apparently distinct from the behaviour of y_ϵ^+. The pipe and channel data show that the magnitudes of $dU^+/d\eta|_{W_{max}}$ and $U_c^+ - U_{W_{max}}^+$ are at first lower than the approximately constant values indicated by the linear curve-fits. For the pipe these lower values are more apparent. There is also evidence of an *overshoot* in these quantities in the pipe over the intermediate Reynolds number range $600 \lesssim \delta^+ \lesssim 3000$. This indicates an elevated mean vorticity at $\eta = 0.5$ and an elevated mean circulation in the outer half of layer IV in the pipe. These behaviours are not seen in the channel data, which apparently settle into their high Reynolds number character sooner than in either the pipe or boundary layer. Different from the pipe and channel, the low δ^+ four layer regime boundary layer $dU^+/d\eta|_{W_{max}}$ values are smaller than at high δ^+, while the values of $U_\infty^+ - U_{W_{max}}^+$ are larger. These behaviours are evident for $\delta^+ \lesssim 2000$.

Comparison of the data in figures 4, 5 and 6m reveals that the outer region vorticity profile development in boundary layers is distinctly different from that in channels or pipes. Consistent with a number of related quantities, the boundary layer data also exhibit greater scatter. This scatter is likely to be associated with factors that are not present in pipes or channels, such as deviations from an exactly zero pressure gradient (in the presence of mean advection). For example, the $dU^+/d\eta|_{W_{max}}$ data of Oweis et al. (2010) (at $\delta^+ \simeq 19000$, 32000 and 47000) indicate values that are discontinuously about 20% lower than the other data in figure 5. On the other hand, their $U_\infty^+ - U_{W_{max}}^+$ data on this same figure indicate values that are in very good agreement with the data from the other boundary layer studies. Taken together, these provide evidence that the mild pressure gradient reported for this study may have modified the shape of the layer IV mean vorticity distribution, but apparently not the total vorticity content of this region.

As described in the manuscript, with increasing Reynolds number the mean vorticity concentrates differently on two increasingly distict domains. At any finite δ^+, slightly more than half of this vorticity is contained in the region $\epsilon y^+ \lesssim 2.6$, with the remainder

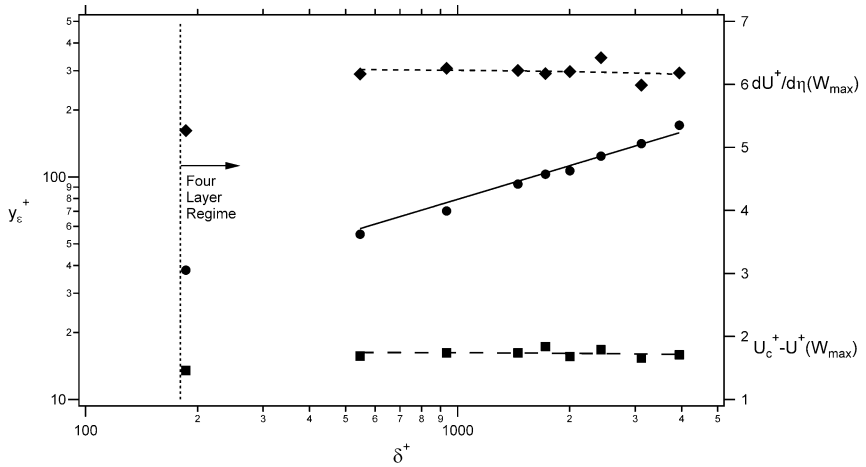

FIGURE 4. Channel flow mean vorticity profile properties versus δ^+, ●; $y_\epsilon^+ = y^+$ position where $dU/dy = u_\tau/\sqrt{\nu\delta/u_\tau}$, ■; $U_c^+ - U^+(y/\delta = 0.5)$, ♦; $dU^+/d\eta(y/\delta = 0.5)$, ——; $y_\epsilon^+ = 2.48\sqrt{\delta^+}$, – – –; $U_c^+ - U^+ = 1.75 - (9.1 \times 10^{-6})y^+$, - - - -; $dU^+/d\eta = 6.24 - (2.1 \times 10^{-5})y^+$. Estimated δ^+ for the onset of the four layer regime is based upon the study of Elsnab et al. (2011).

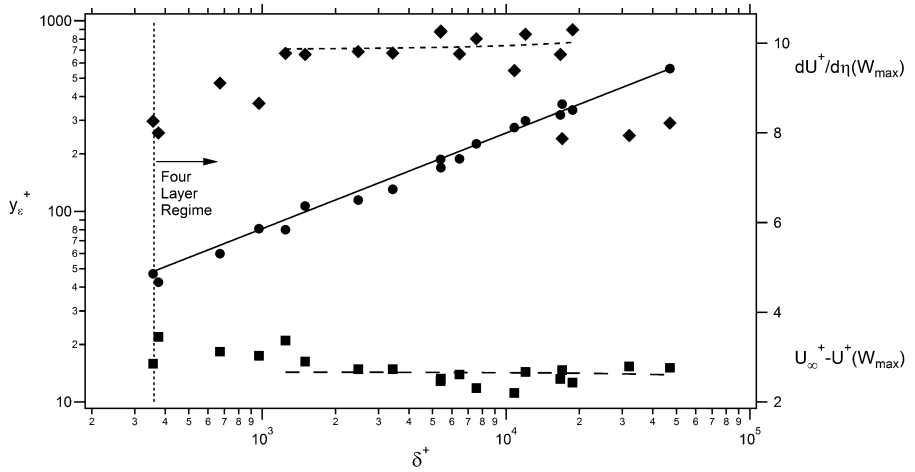

FIGURE 5. Boundary layer mean vorticity profile properties versus δ^+, ●; $y_\epsilon^+ = y^+$ position where $dU/dy = u_\tau/\sqrt{\nu\delta/u_\tau}$, ■; $U_c^+ - U^+(y/\delta = 0.5)$, ♦; $dU^+/d\eta(y/\delta = 0.5)$, ——; $y_\epsilon^+ = 2.53\sqrt{\delta^+}$, – – –; $U_c^+ - U^+ = 2.66 - (1.29 \times 10^{-6})y^+$, - - - -; $dU^+/d\eta = 9.86 + (8.26 \times 10^{-6})y^+$. Estimated δ^+ for the onset of the four layer regime is based upon the study of Klewicki et al. (2011).

being spread over a layer IV domain that approaches δ in width as $\delta^+ \to \infty$. When $|\Omega_z^+|\epsilon^{-1}$ is plotted versus ϵy^+ on linear axes, the profile is increasingly comprised of two spikes of height ϵ^{-1} along the plot axes as depicted in figure 6.

A number of the Ω_z profile properties are more clearly revealed by plotting the normalization of figure 6 on logarithmic axes. This is shown for channel flow in figure 7. On this figure, as well as those for the boundary layer (figure 7m) and the pipe (figure 9), the horizontal dotted line identifies y_ϵ, while the vertical dotted lines identify the upper and lower boundaries of layer III. As indicated, the outer edge of layer II marks the position where, to within the increment of layer I, $\Gamma = \Gamma_c/2$. With increasing δ^+, the Γ contribution from layer I becomes a diminishing fraction of the total. Thus, the

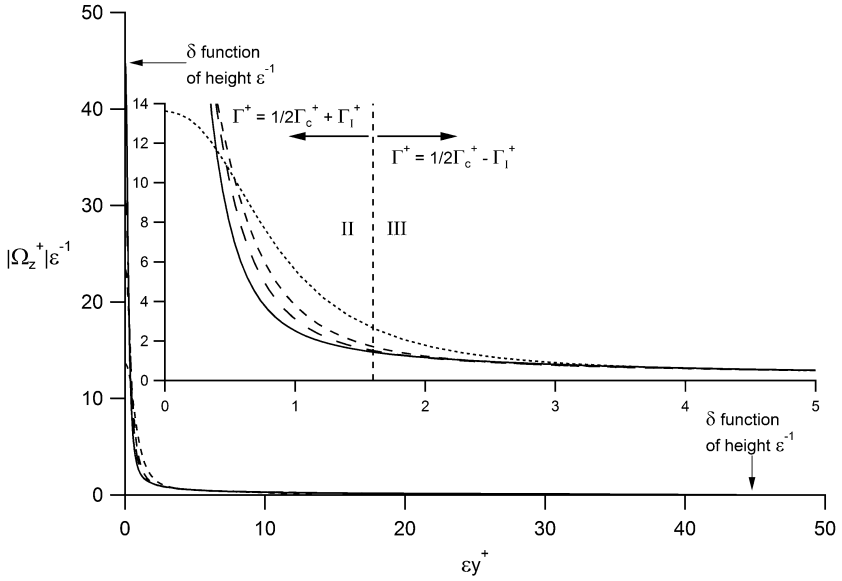

FIGURE 6. Mean vorticity profiles from the channel flow DNS of Hoyas & Jimenez (2006), meso-normalized and plotted on linear axes. Individual profiles are at $\delta^+ = 186, 547, 934$ and 2004.

position where $\Gamma = \Gamma_c/2$ (or equivalently, $U = U_c/2$) approaches the outer edge of layer II ($\epsilon y^+ \simeq 1.6$) as $\delta^+ \to \infty$. Commensurate with the analysis of figure 4, all of the profiles shown in figure 7 convincingly attain an amplitude of 1.0 near the outer edge of layer III. Similarly, logarithmic axes clearly reveal that the limiting values of the profiles are equal to $\epsilon^{-1} = \sqrt{\delta^+}$. Another apparent feature of these profiles is that they exhibit two regions of distinctive negative slope. These are respectively associated with the rapid decay rate of $|\Omega_z|$ near the wall, and the more gradual rate of decay farther from the wall. Lastly, an intriguing feature revealed in figure 7 is that the extensions of the constant slope lines re-intersect the profiles nearly exactly where they first attain their constant limiting values.

In accord with the theory, the outer region of constant slope is well-approximated by $|\Omega_z|\epsilon^{-1} = \phi_c^2/(\epsilon y^+)$, with the best curve fit of the $\delta^+ = 2004$ data over the region extending outward from $\epsilon y^+ \simeq 2.6$ having a downward slope that is slightly less than the $\phi_c^2/(\epsilon y^+)$ function indicated on the graph. In this expression $\phi = \phi_c = 1.6$ as determined by Klewicki et al. (2009). At the onset of the four layer regime ($\delta^+ \simeq 180$) the outer region of approximately constant slope first emerges near the outer edge of layer III, and with increasing δ^+ extends to greater ϵy^+. As indicated, this region of approximately constant slope seems to migrate slightly inward of $\epsilon y^+ = 2.6$ with increasing δ^+. This coincides with the broadening of the T^+ profile across its peak region with increasing δ^+, and the increasing spatial separation between the region of steep downward slope and the position where the VF term loses leading order. The profiles of figure 7 also exhibit a slightly lower magnitude slope in the region just beyond the domain of steeper downward slope. This feature is, however, most recognizable in the high δ^+ pipe flow data discussed below.

The series of profiles in figure 7 reveal that the domain of constant slope closer to the wall moves to smaller ϵy^+ with increasing δ^+. Note that at $\delta^+ = 186$ (i.e., near the onset of the four layer regime) this region extends to the edge of layer III, but as δ^+ increases

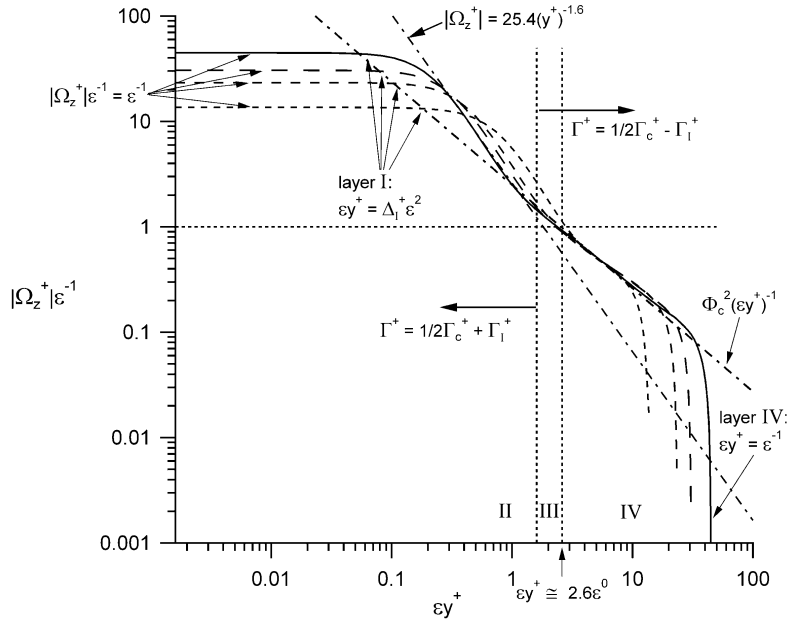

FIGURE 7. Mean vorticity profiles from the channel flow DNS of Hoyas & Jimenez (2006), meso-normalized and plotted on logarithmic axes. Individual profiles are at $\delta^+ = 186, 547, 934$ and 2004; dotted, small dash, large dash and solid lines, respectively. $\phi_c = 1.6$, and Δ_I^+ is the inner-normalized width of layer I.

it becomes embedded deeper within the region where the VF term is of leading order. Thus, at the start of the four layer regime there is no spatial separation at all between the steep near-wall decrease in $|\Omega_z|$, and the more gradual decay rate characterized by the inertially dominated mean dynamics in layer IV. With increasing δ^+ this spatial separation approximately increases like $2.6\sqrt{\delta^+} - 40$ when measured in inner units.

The area under any of the curves in figure 7 is the inner-normalized numerator in (2.1), while U_c^+ has magnitude equaling the inner-normalized denominator. Owing to this, the inner-normalized displacement thickness is simultaneously located closer to the wall and farther from the outer edge of layer III, i.e., deeper within the region where ϕ approximates constancy, as δ^+ increases. The displacement thickness analysis of §2.1.2 used the results in figure 7, the layer scaling properties (table 1m), and the entries in table 3m to develop an accurate estimate for δ^{*+} as a function of δ^+.

Inner-normalized mean vorticity profiles for pipe flow are plotted versus y^+ in figure 8. This figure contains the data of McKeon (2003), along with the $\delta^+ = 1000$ profile from the DNS of Cheng (2011). Over an interior domain, each of these profiles convincingly follow a region of constant downward slope that is close to -1. This is the region associated with a logarithmic-like mean velocity profile, and its existence is consistent with classical scaling arguments as well as the present theory. This region of constant slope, however, extends over a different y^+ range at each δ^+, and for profiles at sufficiently disparate δ^+ the respective regions of constant downward slope extend over y^+ ranges that approach being (or, in fact, become) mutually exclusive. This phenomenon is characterized by the logarithmic zone of the low δ^+ profile residing on a lower y^+ range. The region where $\phi = \phi_c$ most closely approximates constancy initiates near the outer edge of layer III, and this position moves outward in y^+ units like $2.6\sqrt{\delta^+}$. As previously noted by Wei et al. (2005), this structural attribute of the theory connects to experimental

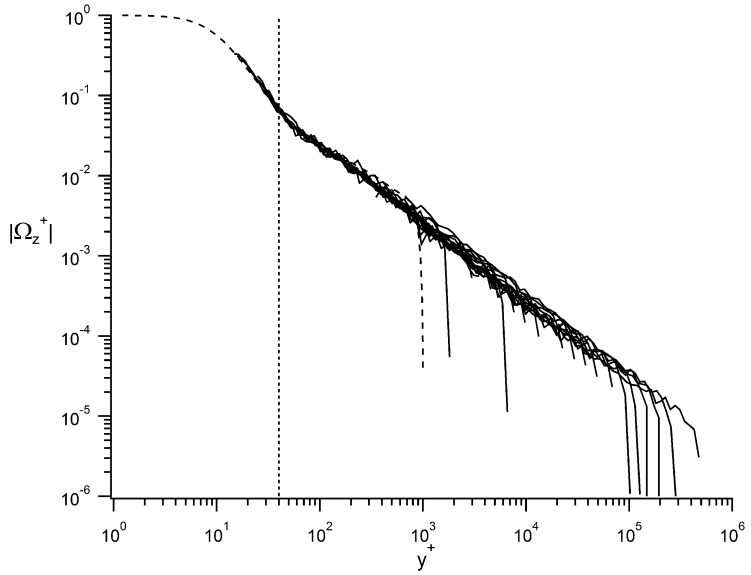

FIGURE 8. Inner-normalized mean vorticity profiles in turbulent pipe flow. Solid lines are from the experiments of McKeon (2003), $1800 \lesssim \delta^+ \lesssim 530000$. Dashed line is from the $\delta^+ = 1000$ DNS of Cheng (2011).

observations indicating that the onset of logarithmic behaviour moves to increasing y^+ values with increasing δ^+ (Zagarola & Smits 1998a; Wosnik et al. 2000; McKeon et al. 2004; Osterlund et al. 1999; Marusic et al. 2013).

The data of figure 8 exemplify the result demonstrated by all of the flows; that the near-wall profile of $|\Omega_z^+|$ is invariant with Reynolds number when plotted versus y^+. The totality of the evidence examined indicates that this region of inner scaling extends to about $y^+ = 40$. This position is indicated by the vertical dotted line on the graph. As can be seen, $y^+ \simeq 40$ coincides with the outermost position of steep downward slope. Beyond this position, the downward slope diminishes, and for the higher δ^+ flows becomes detectably less than the slope at larger y^+. This connects to the pipe flow data presented in Marusic et al. (2013) indicating that the logarithmic mean profile is approached from below at large δ^+. McKeon et al. (2004) identify a domain in the pipe that is beyond the traditionally defined buffer layer and interior to the onset of a logarithmic profile where they find that the mean velocity follows a power law dependence. In the context of the present description, this is the region $40 \lesssim y^+ \lesssim 2.6\epsilon^{-1}$.

Figure 9 presents $|\Omega_z^+|\epsilon^{-1}$ versus ϵy^+ for the $\delta^+ = 500$ and 1000 profiles from the DNS of Cheng (2011), along with profiles of McKeon (2003). As with figure 7, the vertical dotted lines indicate the upper and lower boundaries of layer III, while the position where the profile crosses the horizontal dotted line denotes y_ϵ^+ (see table 3m). Owing to the diminishing physical size of the viscous length with increasing Reynolds number, only the lower δ^+ profiles contain data in the region $y^+ < 40$. Thus, the apparent invariance of the near-wall profiles under inner-normalization is used to generate profiles in this region at higher δ^+. These reconstructed estimates are given by dotted lines, and have been reproduced for the selection of δ^+ values given in the figure caption. The data support inner scaling out to $y^+ \simeq 40$. Thus, at any given δ^+ the reconstructed profile is only valid out to 40ϵ, although for visual appearance they are extended to greater ϵy^+ on the figure.

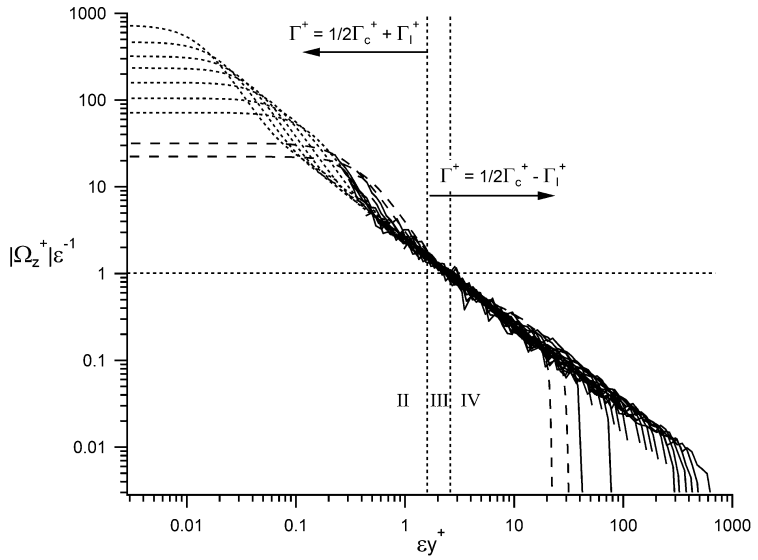

FIGURE 9. Mean vorticity profiles in turbulent pipe flow, meso-normalized and plotted on logarithmic axes. Solid lines are from the experiments of McKeon (2003), $1800 \lesssim \delta^+ \lesssim 530000$. Dashed lines are from the $\delta^+ = 500$ and 1000 simulations of Cheng (2011). Dotted lines are from the near-wall $\delta^+ = 1000$ DNS, and have been transformed to correspond to the experimental profiles at $\delta^+ = 5108, 10914, 25279, 102200, 216980$ and 530030.

This last point connects to the aforementioned spatial separation between the region of inner scaling and the position where the VF term loses dominant order in (1.1m). As clearly shown by the normalization of figure 9, the *knee* in the profile associated with the change from the steep downward slope moves to smaller ϵy^+ with increasing δ^+. The data of figure 8, however, give an indication that the flattening of the profile just after $y^+ = 40$ is at most a weak function of δ^+. We add to this the theoretical finding that $y_\epsilon^+ = \xi\epsilon^{-1}$, where it is empirically shown that $\xi \simeq 2.6$ (see table 3m). Collectively, these considerations indicate that the value of $|\Omega_z^+|$ is (nominally) invariant at $y^+ \simeq 40$, while the value of $|\Omega_z^+|\epsilon^{-1}$ equals unity at $\epsilon y^+ \simeq 2.6$. With Reynolds number these two end-points move apart according to $\Delta y^+ \simeq 2.6\sqrt{\delta^+} - 40$. Thus, if the flattened portion of the profile (just after $y^+ = 40$) is invariant under inner-normalization, then the inner normalized profile between the end-points of this domain is a function of δ^+. This feature varies weakly with δ^+. According to the theory the inner normalized mean profile in this region approaches invariance as $\delta^+ \to \infty$, but apparently more slowly than does the profile in the region of $\phi = \phi_c$ similarity. The divergence of the ϕ profiles beyond $y^+ = 40$ but interior to $\epsilon y^+ \simeq 2.6$ (Klewicki 2013a), supports the existence of this weak δ^+ dependence.

As with the channel data, all of the pipe flow profiles of figure 9 convincingly pass through unity at $\epsilon y^+ \simeq 2.6$. These data verify this property over the range $500 \lesssim \delta^+ \lesssim 530000$. The region beyond the outer edge of layer III is also seen to mark where each of the profiles most accurately approximates a constant downward slope having a value close to -1. This is the domain where self-similar dynamics are approximated by $\phi = \phi_c$ as $\delta^+ \to \infty$.

2.1.4. *Mean Circulation Apportionment*

We now derive relations that describe the rates of Γ accumulation on each of the four layers as δ^+ is varied. These begin with the relations developed by Klewicki (2013a). According to the scaling properties of the four layer structure (table 1m), the rate of change of the inner-normalized increments in mean circulation per unit length across layers II and IV (or equivalently the increments in mean velocity) with Reynolds number are given by

$$\frac{d\Gamma^+_{II}}{d\delta^+} = \frac{d\Gamma^+_{IV}}{d\delta^+} \simeq 0.5\frac{d\Gamma^+_e}{d\delta^+}, \tag{2.3}$$

where Γ^+_e refers to either Γ^+_c or Γ^+_∞. The theory also indicates that the Γ^+ increments across layers I and III are, in order of magnitude, fixed for all δ^+. From this, one readily surmises that increments in inner-normalized mean velocity associated with increases in δ^+ are solely added to layers II and IV.

How these mean circulation increments accumulate within layers II and IV is clarified by considering $d\Gamma^+_{II}/d\Delta^+_{II}$ and $d\Gamma^+_{IV}/d\Delta^+_{IV}$, where, Δ^+_{II} and Δ^+_{IV} are the inner normalized thicknesses of layers II and IV, which are also Reynolds number dependent. The growth rates of layers II and IV with δ^+ are respectively given by

$$\frac{d\Delta^+_{II}}{d\delta^+} = \frac{0.8}{\sqrt{\delta^+}}, \tag{2.4}$$

and

$$\frac{d\Delta^+_{IV}}{d\delta^+} = 1 - \frac{1.3}{\sqrt{\delta^+}} \tag{2.5}$$

Klewicki (2013a). Combining (2.3) with (2.4) yields

$$\frac{d\Gamma^+_{II}}{d\delta^+}\frac{d\delta^+}{d\Delta^+_{II}} = \frac{d\Gamma^+_{II}}{d\Delta^+_{II}} = \frac{5\sqrt{\delta^+}}{8}\frac{d\Gamma^+_e}{d\delta^+} = (\epsilon\phi_c)^{-1}\frac{d\Gamma^+_e}{d\delta^+}, \tag{2.6}$$

where, in the last equality we use $\epsilon = 1/\sqrt{\delta^+}$, and the value of $\phi_c = 1.6$ as determined by Klewicki et al. (2009). Equation 2.6 indicates that with increasing Reynolds number the circulation in layer II increases at a rate that is $\sqrt{\delta^+}$ times the rate at which the total circulation (per unit length) accumulates within the flow as a whole. This property underlies the development of the near-wall spike in Ω_z shown in figure 6, and is characteristic of the near-wall $\phi = O(1) \neq$ constant self-similarity. This is associated with the mechanism of vorticity stretching described later. This mechanism affects scale separation between the velocity and vorticity field motions by causing a rate of reduction in the scale of the vortical motions that out-paces the rate at which the layer II width is decreasing relative to δ, see (2.16) below.

Similarly, combining (2.3) with (2.5) yields

$$\frac{d\Gamma^+_{IV}}{d\delta^+}\frac{d\delta^+}{d\Delta^+_{IV}} = \frac{d\Gamma^+_{IV}}{d\Delta^+_{IV}} = \frac{0.5\sqrt{\delta^+}}{(\sqrt{\delta^+} - 1.3)}\frac{d\Gamma^+_e}{d\delta^+}, \tag{2.7}$$

and thus as $\delta^+ \to \infty$

$$\frac{d\Gamma^+_{IV}}{d\Delta^+_{IV}} \to 0.5\frac{d\Gamma^+_e}{d\delta^+}. \tag{2.8}$$

Equation 2.7 indicates that with increasing δ^+, Γ^+_{IV} accumulates (in layer IV) at the

same rate that Γ_e^+ accumulates within the entire flow. This is associated with $\Delta_{IV} \to \delta$ as $\delta^+ \to \infty$. The direct proportionality is a consequence of the layer IV vorticity dispersion mechanism described in the manuscript.

The above analysis clarifies that increments in Γ^+ associated with increases in δ^+ solely occur in layers II in IV, and further describes the relative rates at which these increments accumulate. The theoretically determined decay rates of $|\Omega_z|$ described in the manuscript also reveal that for sufficiently high δ^+ only the portion of layer IV between $\epsilon y^+ \simeq 2.6$ and $y/\delta \simeq 0.5$ exhibits increases in Γ^+ with increasing δ^+. Similarly, analyses of the mean vorticity profile indicate that the lower portion of layer II ($y^+ \lesssim 40$) has a fixed Γ^+. Thus, only the portion of layer II between $y^+ \simeq 40$ and $\epsilon y^+ \simeq 1.6$ accumulates Γ^+ with increasing δ^+.

It may be shown that

$$\frac{dU^+}{dy^+} = \frac{\phi_c^2}{(y^+ - C)}, \tag{2.9}$$

holds on the domain where $\phi = \phi_c$ (Fife et al. 2009; Klewicki et al. 2009; Klewicki 2013a). Integration of (2.9) yields a mean profile that is approximated by the logarithmic function

$$U^+ = \phi^2 \ln(y^+ - C) + D, \tag{2.10}$$

with increasing accuracy as $\delta^+ \to \infty$. Thus, relative to describing the rate at which Γ_e^+ accumulates within a layer of thickness δ^+, the present theory attaches logarithmic growth to this outer portion of the L_β hierarchy.

The traditional way of describing $U_e^+ = -\Gamma_e^+$ as a function of δ^+ uses a logarithmic equation of the form

$$U_e^+ = A_1 \ln(\delta^+) + B_1. \tag{2.11}$$

In (2.11) A_1 is the inverse of the von Kármán constant, and B_1 is made up of the sum of an invariant near-wall contribution and a wake contribution that, at sufficiently high δ^+, is also constant, e.g., Monkewitz et al. (2008).

While the present theory attributes Γ^+ increments to both layers II and IV, it also specifies that the layer IV contribution is most accurately described by a logarithmic function. Recent pipe and boundary layer data at large δ^+ support this prediction (Marusic et al. 2013). Accordingly, one can write

$$U_e^+ = |\Gamma_I^+| + |\Gamma_{II}^+| + |\Gamma_{III}^+| + \frac{4}{A^2} \ln\left(\frac{\delta^+/2 - 7}{2.6\sqrt{\delta^+} - 7}\right) + (U_e^+ - U_{W_{max}}^+), \tag{2.12}$$

where in this expression $A = A(\beta)$, and the offset C in (2.10) is set to the estimate of 7 described in the manuscript, also see Klewicki (2013a). Noting that Γ_I^+ and Γ_{III}^+ are constants, $|\Gamma_{II}^+| \simeq 0.5 U_e^+$, and at sufficiently high δ^+ $(U_e^+ - U_{W_{max}}^+)$ becomes constant (see figures 6m, 4 and 5), allows (2.12) to be written as

$$\frac{U_e^+}{2} = A_2 \ln\left(\frac{\delta^+/2 - 7}{2.6\sqrt{\delta^+} - 7}\right) + B_2. \tag{2.13}$$

Figures 10a,b present channel, pipe, and boundary layer data plotted and fit according to (2.11) and (2.13) respectively. As indicated in figure 10a, the curve-fits were only applied to data that are significantly within the four layer regime. The differences between the curve-fits in figures 10 are not detectable by visual inspection. The difference is that (2.11)

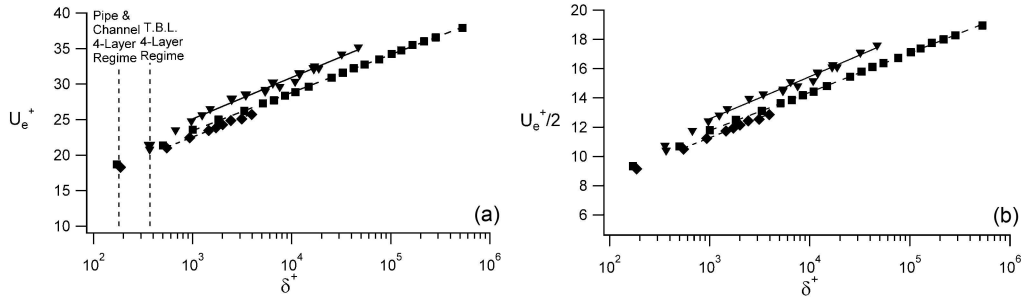

FIGURE 10. Measures of maximum mean velocity, U_e^+ (U_c^+ or U_∞^+), as a function of δ^+, boundary layer, ▼; channel flow, ♦; pipe flow, ■, (a) plotted according to (2.11), (b) plotted according to (2.13).

Flow	Reynolds Number Range	A_1 (A_1^{-1})	B_1	A_2 (A_2^{-1})	B_2
Channel	$540 \lesssim \delta^+ \lesssim 4000$	2.372 (0.422)	6.161	2.514 (0.398)	6.645
Pipe	$1000 \lesssim \delta^+ \lesssim 530000$	2.321 (0.431)	7.420	2.369 (0.422)	7.319
Boundary Layer	$1000 \lesssim \delta^+ \lesssim 50000$	2.525 (0.395)	7.633	2.614 (0.383)	7.661

TABLE 1. Coefficients in (2.11) and (2.13) determined by fitting the data presented in figure 10.

attributes logarithmic dependence to an internal region that extends from $O(\nu/u_\tau)$ to $O(\delta)$, while (2.13) only accounts for it on the domain where $\phi = \phi_c$. This difference is apparent in the curve-fit parameters listed in table 1. Specifically, the values for the inverse of the leading coefficient are consistently larger for the curve-fit based on (2.11). On the other hand, fitting the channel data to (2.13) yields a value that is only about 1.7% different from that determined by Klewicki et al. (2009) at $\delta^+ = 2004$. Similarly, the pipe data fit to (2.13) yields a slope that is essentially identical to that found by McKeon (2003), and for the boundary layer, identical to the estimate reported by Nagib & Chauhan (2008). These studies used different techniques on the same data sets. A common element, however, is that in each case the region of logarithmic dependence was taken to begin at a position farther from the wall than implicitly assumed by fitting to (2.11). The present theory provides a precise specification for the Reynolds number dependent position where a logarithmic profile is most accurately approximated, and this corresponds to the Γ^+ increments on the hierarchy portion of layer IV.

If $U_e^+/2$ is logarithmic as described by (2.13), then according to the theory so is the growth rate of $-\Gamma_{II}^+ \simeq U_e^+/2$. Thus, the small difference between the slopes determined by (2.11) and (2.13) is not in the overall rate of change of Γ^+ in the region interior to $\epsilon y^+ \lesssim 2.6$, but rather in where and how it occurs in this region. This has to do with the profile variation in the region $\epsilon 40 \lesssim \epsilon y^+ \lesssim 2.6$. In the context of the theory, this is the region where the length scale (figure 1m) required to write the mean dynamical equation in its self-similar form transitions from its steeper near-wall slope to its constant slope (beginning beyond $\epsilon y^+ \simeq 2.6$) that is characteristic of the logarithmic behavior accounted for in (2.13). In figures 2m and 3m, this is where the vorticity transport contribution to dT^+/dy^+ gains parity with and subsequently exceeds the vorticity stretching contribution.

Considering (2.13) under the condition, $\delta^+ \to \infty$, allows the small effect of the offset,

$C = 7$, to be neglected. After some algebraic manipulation, its differentiation with respect to δ^+ yields

$$\frac{d|\Gamma_e^+|}{d\delta^+} = \frac{\phi_c^2}{\delta^+}. \tag{2.14}$$

Combining (2.14) with (2.8) gives

$$\frac{d|\Gamma_{IV}^+|}{d\Delta_{IV}^+} = \frac{(\epsilon\phi_c)^2}{2}. \tag{2.15}$$

While (2.8) gives the Γ^+ accumulation rate in layer IV relative to that in the layer as a whole, (2.15) gives its absolute growth rate. Similarly, combining (2.14) with (2.6) gives

$$\frac{d|\Gamma_{II}^+|}{d\Delta_{II}^+} = \epsilon\phi_c. \tag{2.16}$$

This is the absolute growth rate of Γ^+ in layer II. Regarding (2.6) and (2.16), ϕ_c apparently has relevance to (2.16), even though the $\phi_c \simeq$ constant similarity begins near $\epsilon y^+ = 2.6$. This is theoretically reconciled via (2.3). Physically, it points to a self-similar inner-outer interaction. A key attribute of the inner-outer interaction is that it embodies the mechanistically equivalent processes that simultaneously support the wallward transport of mean momentum and the outward transport of mean vorticity (Klewicki et al. 2007; Eyink 2008). Under such an interaction, the scale and intensity of the vortical motions in layer II adjust (as a function of δ^+) in concert with the vorticity intensity and scale in layer IV, such that (independent of δ^+) the scale separation at the outer edge of layer II (induced by vorticity stretching in layer II) equilibrates with the onset of vorticity dispersion induced scale separation that becomes predominant starting near the inner edge of layer IV.

2.2. *Properties of the vorticity fluctuations*

This section augments those parts of the paper associated with the properties of the vorticity fluctuations.

2.2.1. *Ratio of rms to mean spanwise vorticity*

The boundary layer profiles of figure 11 exhibit similar properties as just described for the channel in figure 10m. The inner region of these profiles is essentially indistinguishable from the channel. In particular, the region of steep increase is observed to have the same slope. It is clear, however, that the outer region of constant slope develops differently than in the channel. In comparing the boundary layer and channel it should be noted that the maximum δ^+ value in figure 11 is only about 65% of that in figure 10m, and that at equal δ^+ these flows are at different stages of evolution relative to the onset of the four layer regime (figure 1).

2.2.2. *Vorticity stretching and exchange*

Here we clarify how the mechanisms of vorticity stretching and exchange are related to the layer II scale separation phenomena depicted in figure 3m.

The mean vorticity is dominant near the wall. By $y^+ \simeq 20$, however, the intensities of all three components attain magnitudes that are about equal to the mean (Klewicki 1997). As exemplified by figures 10m and 11, interior to $y^+ \simeq 15$ the instantaneous vorticity dynamics are dominated by Ω_z, and beyond $y^+ \simeq 40$ the fluctuations are, on average, larger.

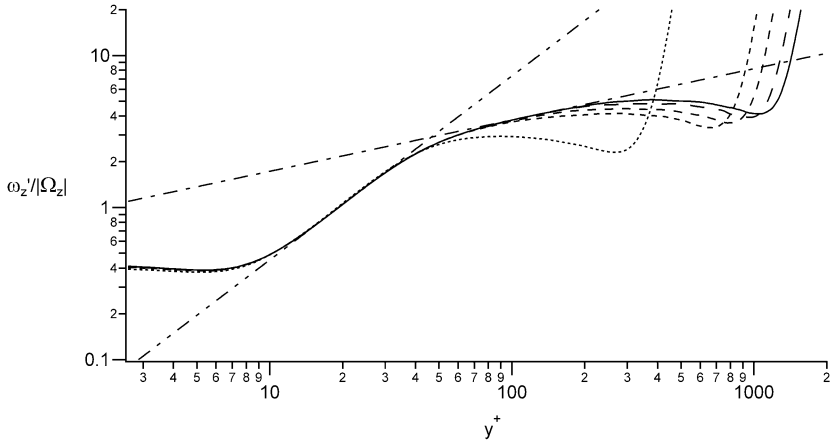

FIGURE 11. Spanwise vorticity intensity profiles from the boundary layer DNS of Schlatter & Orlu (2010), normalized by $|\Omega_z|$ and plotted versus y^+, $\delta^+ = 359$, · · ·; $\delta^+ = 830$, - - -; $\delta^+ = 974$, – – –; $\delta^+ = 1145$, — — —; and $\delta^+ = 1271$, ——. Curve-fit in Layer II is given by $\omega_z'/|\Omega_z| = 0.027(y^+)^{1.21}$. Curve-fit in layer IV is given by $\omega_z'/|\Omega_z| = 0.796(y^+)^{0.34}$.

How this transition takes place is clarified by examining the transport equation for the mean enstrophy. Its inner-normalized form is given by

$$0 = \Omega_z^+ \left(\frac{\partial \langle w\omega_y \rangle^+}{\partial y^+} - \frac{\partial \langle v\omega_z \rangle^+}{\partial y^+} \right) + \frac{\partial^2 (\frac{1}{2}{\Omega_z^+}^2)}{\partial {y^+}^2} - \left(\frac{\partial \Omega_z^+}{\partial y^+} \right)^2 \tag{2.17}$$

which is exact for channel or pipe flow. The last two terms on the right of (2.17) respectively represent the viscous diffusion and dissipation of mean enstrophy. As noted relative to equation 1.2m, to within the boundary layer approximation

$$\langle w\omega_y \rangle - \langle v\omega_z \rangle = \frac{\partial \langle uv \rangle}{\partial y} = -\frac{\partial T}{\partial y}, \tag{2.18}$$

and thus the first term on the right of (2.17) is associated with the variation of the TI term in the mean momentum equation. This term in (2.17) is analogous to the production term in the equations for mean and turbulence kinetic energy, as it is associated with the exchange between Ω_z^2 and $\langle \omega_i^2 \rangle$ ($i = 1, 2, 3$), e.g., Tennekes & Lumley (1972). Vorticity stretching is the relevant physical mechanism, as it underlies a rapid three-dimensionalization of the instantaneous vorticity field with increasing distance from the wall. Like the transport equation for $\langle u^2 \rangle$, that for $\langle \omega_z^2 \rangle$ (not shown) solely contains this exchange term, only with a negative sign. Thus, in a time averaged sense, $\langle \omega_z^2 \rangle$ is the *conduit* through which the loss of mean enstrophy is transferred to the other fluctuating vorticity components. This transfer also occurs via vorticity stretching and reorientation (Tennekes & Lumley 1972).

A number of features are apparent in figures 12a,b, with the overarching observation being that the mean enstrophy transport mechanisms in the region $y^+ \lesssim 40$ are essentially identical in all of the canonical wall-flows. Note, however, that in the region $y^+ \lesssim 1$ the $\delta^+ = 2004$ channel profile differs slightly from channels at lower δ^+ (figure 12a), and from pipes and boundary layers at $\delta^+ \simeq 1000$ (figure 12b). Interior to $y^+ \simeq 2.6$, (2.17) is nearly perfectly balanced by the diffusion and turbulence exchange terms. These terms attain essentially equal and opposite maxima at the outer edge of layer I ($y^+ \simeq 2.6$). Beyond this point, the dissipation term becomes non-negligible, and the diffusion and

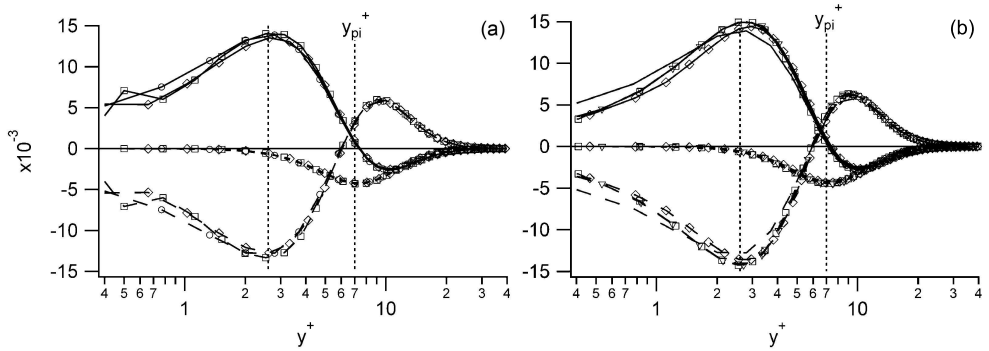

FIGURE 12. Near-wall inner normalized mean enstrophy budgets for turbulent wall flows, mean to turbulence exchange, ——; viscous diffusion, — — —; viscous dissipation, – – –. (a) channel flows of Hoyas & Jimenez (2006), $\delta^+ = 547$, ◇; $\delta^+ = 934$, □; $\delta^+ = 2004$, ○, (b) $\delta^+ = 1020$ channel flow DNS of Abe et al. (2004), ◇; $\delta^+ = 1142$ pipe flow DNS of Wu & Moin (2008), □; $\delta^+ = 1245$ boundary layer DNS of Schlatter & Orlu (2010), ▽; $\delta^+ = 2004$ channel flow DNS of Hoyas & Jimenez (2006); no symbol.

exchange terms rapidly decrease. The start of the L_β hierarchy coincides with a zero-crossing in the turbulence exchange term. This must be the case since the TI term attains its maximum at this position. The dissipation of mean enstrophy is maximal at this point, and is essentially balanced by the now positive diffusion term which passes through zero near $y^+ = 6$. The diffusion term peaks near $y^+ = 10$, and beyond that point the turbulence exchange and dissipation profiles merge to provide similar magnitude negative contributions that together balance the diffusion term. For greater y^+ the profiles decrease in magnitude, and by $y^+ \simeq 40$ they attain values that are small in comparison to near the wall.

The turbulence exchange term is positive and increasing out to $y^+ \simeq 2.6$, and thus the mean enstrophy is enhanced by the turbulence. This occurs owing to the constraint imposed by the no-slip boundary condition. Unlike away from the wall, streamwise velocity fluctuations in this region directly (and with negligible loss) contribute to $\tilde{\omega}_z$, and thus also to its average, Ω_z. This interpretation is substantiated by the essentially zero value of the dissipation term in layer I. Between the outer edge of layer I and the start of the L_β hierarchy ($y^+ = y_{pi}^+ \simeq 7$), this direct connection is diminished, albeit the net exchange is still from the turbulence to the mean. Consistent with this, the dissipation term acquires the largest magnitude of the three terms in (2.17) near y_{pi}^+. Beyond y_{pi}^+, the turbulence exchange term acts like a sink in (2.17), or equivalently, the mean enstrophy acts like a source to the fluctuating enstrophy. This is where the $\omega_z'/|\Omega_z|$ profiles of figures 10m and 11 begin to exhibit their rapid layer II increase. Physically, mean enstrophy is being converted into $\langle\omega_z^2\rangle$ which, by the processes of vorticity stretching and reorientation, is rapidly transferred to $\langle\omega_x^2\rangle$ and $\langle\omega_y^2\rangle$ (see figures 11m and 12m).

The distance between layer I ($y^+ \simeq 2.6$) and the onset of the hierarchy ($y^+ = y_{pi}^+ \simeq 7$) is interpreted to be where Ω_z loses its boundary condition related correlation with ω_z. This loss of correlation is due to the inertial mechanism embedded in the turbulence exchange term of (2.17). It is thus expected that the scale of this turbulence mechanism should be about the width of this region, or slightly greater than 4 viscous units. The $W^+(y^+)$ distribution quantifies the average length scale of this mechanism. Figure 1m shows that $W^+(y^+)$ is minimal $\simeq 4.1$ precisely at $y^+ = y_{pi}^+$. Consistently, the minimum value of $W\omega_z'/u_\tau \simeq 1.15$ (figure 9m) also occurs at $y^+ = y_{pi}^+$.

The above description of how the vorticity field three-dimensionalizes is supported by

the channel results of figure 11m, and the channel and boundary layer results of figure 12m. At the outer edge of layer I the $W\omega_x'/u_\tau$ values are near unity, and from there they decrease to a minimum near $y^+ = 6$. In this region of the flow, the $W\omega_x'/u_\tau$ profiles from the channel exhibit a slight Reynolds number dependence, but with increasing distance from the wall the variations between the different δ^+ profiles diminish. Beyond about $y^+ \simeq 40$ these variations are undetectable for the range of Reynolds numbers considered. Whether this behaviour is retained at higher δ^+ is currently unknown. Beyond $y^+ \simeq 40$, the $W\omega_x'/u_\tau$ profiles exhibit features that are highly similar to those those of $W\omega_z'/u_\tau$ in figure 11m. The $W\omega_y'/u_\tau$ profiles provide evidence of an emerging invariance from the wall to the end of the L_β hierarchy ($y/\delta \simeq 0.5$).

Figure 12m compares the $W\omega_i'/u_\tau$ for the channel at $\delta^+ = 2004$ and in the boundary layer at $\delta^+ = 1271$. Effectively, these figures portray the process by which the vorticity field becomes three dimensional, as described in terms of the length scale intrinsic to the mechanism of turbulent inertia. Consistent with the analysis of (2.17), interior to $y^+ \simeq 40$ the spanwise component is largest. Near this location, however, all three component intensities gain approximate parity, and each is about three times greater than $|\Omega_z|$ (see figures 10m and 11). For $y^+ \simeq 40$, the $W\omega_x'/u_\tau$ profile slightly exceeds the other two. By $\epsilon y^+ \simeq 2.6$ $W\omega_x'/u_\tau$ is essentially parallel to but slightly greater than $W\omega_y'/u_\tau$ and $W\omega_z'/u_\tau$. This feature persists to the end of the hierarchy ($y/\delta \simeq 0.5$). Near the zero crossing of the TI term (position of maximum $-\langle uv\rangle^+$, y_m^+), the $W\omega_y'/u_\tau$ profile exactly melds with the $W\omega_z'/u_\tau$ profile, and beyond that point, the two profiles are indistinguishable. This is true for both the channel and the boundary layer. Beyond the outer edge of layer III, all of the channel profiles on figure 12m(a) convincingly attain the same slope, as do the boundary layer profiles of figure 12m(b). This slope, however, is not the same the channel and boundary layer at the given Reynolds numbers. In combination, the present theory, mean enstrophy analysis, and results of figures 11m and 12m support the emergence of a self-similar vorticity three-dimensionalization process. This process is characteristic of the $\phi \neq$ constant similarity structure on the portion of the L_β hierarchy interior to $\epsilon y^+ \sim 2.6$ (Klewicki 2013a). Beyond layer III, these evidences also support the existence of self-similar vorticity dispersion as depicted in figure 10m.

REFERENCES

Abe, H, Kawamura, H. & Matsuo, Y. 2004 Surface heat-flux fluctuations in a turbulent channel flow up to $Re_\tau = 1020$ with Pr = 0.025 and 0.71. *Int. J. Heat and Fluid Flow* **25**, 404–419.

Cheng, C. 2011 Numerical study of internal wall-bounded turbulent flows. PhD thesis, University of Melbourne, Victoria, Australia.

Elsnab, J., Klewicki, J., Maynes, D. & Ameel, T. 2011 Mean dynamics of transitional channel flow. *J. Fluid Mech.*, **678**, 451–481.

Eyink G. 2008 Turbulent flow in pipes and channels as cross-stream "inverse cascades" of vorticity. *Phys. Fluids* **20**, 125101.

Fife, P., Klewicki, J. & Wei, T. 2009 Time averaging in turbulence settings may reveal an infinite hierarchy of length scales. *J. of Discrete and Continuous Dynamical Systems*, **24**, 781–807.

Hoyas, S. & Jimenez, J. 2006 Scaling the velocity fluctuations in turbulent channels up to $Re_\tau = 2003$. *Phys. Fluids* **18**, 011702.

Klewicki, J.C. 1997 Self-sustaining traits of near-wall motions underlying boundary layer stress transport. In *Self-Sustaining Mechanisms of Wall Turbulence* (ed. R. Panton), pp. 135–166. Computational Mechanics Publications, Southampton, UK.

Klewicki, J., Fife, P., Wei, T. & McMurtry, P. 2007 A physical model of the turbulent

boundary layer consonant with mean momentum balance structure. *Phil. Trans. Roy. Soc. A* **365**, 823–839.

Klewicki, J., Fife, P. & Wei, T. 2009 On the logarithmic mean profile. *J. Fluid Mech.*, **638**, 73–93.

Klewicki, J., Ebner, R. & Wu, X. 2011 Mean dynamics of transitional boundary-layer flow. *J. Fluid Mech.*, **682**, 617–651.

Klewicki, J., Chin, C., Blackburn, H., Ooi, A. & Marusic, I. 2012 Emergence of the four layer dynamical regime in turbulent pipe flow. *Phys. Fluids*, **24**, 045107.

Klewicki, J.C. 2013a Self-similar mean dynamics in turbulent wall-flows *J. Fluid Mech.*, **718**, 596–621.

Laadhari, F. 2011 An apparent symmetry property of the mean velocity gradient in turbulent Poiseuille flows and its implications. *Phys. Fluids* **23**, 101705.

Marusic, I., Monty, J., Hultmark, M. & Smits, A. 2013 On the logarithmic region in wall turbulence. *J. Fluid Mech.* **716**, R3.

McKeon, B.J. 2003 High Reynolds number turbulent pipe flow. PhD thesis, Princeton University, Princeton, New Jersey.

McKeon, B., Li, J., Jiang, W., Morrison, J. & Smits, A. 2004 Further observations on the mean velocity distribution in fully-developed turbulent pipe flow. *J. Fluid Mech.* **501**, 135–147.

Monkewitz, P.A., Chauhan, K.A. & Nagib, H.M. 2008 Comparison of mean flow similarity laws in zero pressure gradient turbulent boundary layers. *Phys. Fluids* **20**, 105102.

Nagib, H.M. & Chauhan, K.A. 2008 Variation of von Karman coefficient in canonical flows. *Phys. Fluids* **20**, 101518.

Osterlund, J.M., Johansson, A.V., Nagib, H.M. & Hites, M.H. 1999 Wall shear stress measurements in high Reynolds number boundary layers from two facilities. In proceedings *In 30th AIAA Fluid Dynamics Conf.*, Norfolk, VA.

Oweis, G.F., Winkel, E.S., Cutbrith, J.M., Ceccio, S.L., Perlin, M., Dowling, D.R. 2010 The mean velocity profile of a smooth-flat-plate turbulent boundary layer at high Reynolds number. *J. Fluid Mech.* **665**, 357–381.

Schlatter, P. & Orlu, R. 2010 Assessment of direct numerical simulation data of turbulent boundary layers. *J. Fluid Mech.* **659**, 116–126.

Tennekes, H. & Lumley, J. 1972 A First Course in Turbulence. MIT Press, Cambridge.

Wei, T., Fife, P., Klewicki, J. & McMurtry, P. 2005 Properties of the mean momentum balance in turbulent boundary layer, pipe and channel flows. *J. Fluid Mech.* **522**, 303–327.

Wosnik, M., Castillo, L. & W.K. George 2000 A theory for turbulent pipe and channel flows. *J. Fluid Mech.* **421**, 115–145.

Wu, X., & Moin, P. 2008 A direct numerical simulation study on the mean velocity characteristics in turbulent pipe flow. *J. Fluid Mech.* **608**, 81–112.

Zagarola, M.V. & Smits, A.J. 1998a Mean-flow scaling of turbulent pipe flow. *J. Fluid Mech.* **373**, 33–79.

Zagarola, M.V. & Smits, A.J. 1998b A new mean velocity scaling for turbulent boundary layers. *ASME paper no. FEDSM98-4950.*